A high-performance, metallodielectric 2D photonic crystal for thermophotovoltaics

Solar Energy Materials & Solar Cells 238 (2022) 111536

Contents lists available at ScienceDirect

Solar Energy Materials and Solar Cells

journal homepage: www.elsevier.com/locate/solmat

A high-performance, metallodielectric 2D photonic crystal for thermophotovoltaics

Reyu Sakakibara [a,b,*], Veronika Stelmakh [c], Walker R. Chan [a,c], Robert D. Geil [d], Stephan Krämer [e], Timothy Savas [f,g], Michael Ghebrebrhan [h], John D. Joannopoulos [a,i], Marin Soljačić [i], Ivan Čelanović [a]

[a] Institute for Soldier Nanotechnologies, Massachusetts Institute of Technology, Cambridge, MA, United States
[b] Department of Electrical Engineering and Computer Science, Massachusetts Institute of Technology, Cambridge, MA, United States
[c] Mesodyne Inc., Somerville, MA, United States
[d] Chapel Hill Analytical & Nanofabrication, Laboratory, University of North Carolina, Chapel Hill, NC, United States
[e] Harvard University Center for Nanoscale Systems (CNS), Harvard University, Cambridge, MA, United States
[f] Research Laboratory of Electronics, Massachusetts Institute of Technology, Cambridge, MA, United States
[g] LumArray, Inc., Somerville, MA, United States
[h] U.S. Army Natick Soldier Research, Development, and Engineering Center, Natick, MA, United States
[i] Department of Physics, Massachusetts Institute of Technology, Cambridge, MA, United States

ARTICLE INFO

Keywords:
Thermophotovoltaics
Photonic crystal
Thermal emitter
Selective emitter

ABSTRACT

Fuel-combustion-based thermophotovoltaic (TPV) systems are emerging as a viable power source for small, portable generators for a spectrum of applications such as UAVs, robotic platforms, and sensors. In TPV systems, an emitter heated to above 1000 K emits radiation that is then converted to electricity by a low bandgap photovoltaic cell. One promising class of TPV emitters are two-dimensional photonic crystals (PhCs) made of tantalum, which have shown high-temperature stability at 1150–1250K over hundreds of hours [1,2] and have been implemented in a prototype system with 4.4% fuel-to-electricity efficiency [1]. Tantalum PhCs filled and capped with hafnium oxide can enable even higher optical performance with in-band emissivities of 0.8–0.9. However, two key features are difficult to realize simultaneously: a uniformly filled cavity and a thin capping layer of hafnium oxide [3,4]. Here, we present a process that results in reduced roughness and better thickness control of the capping layer. We use room temperature reflectance measurements and full system simulations to estimate system performance gains. This selective emitter paves the way toward efficient, practical, and portable mesoscale generators.

1. Introduction

Fuel-combustion-based thermophotovoltaic (TPV) systems are promising for addressing the need for mesoscale portable generators with power output of 1-100 W. With the current state of the art, one must either take several lithium ion batteries (~100 mW) or a bulky diesel generator (~1 kW). However, lithium ion batteries are approaching their theoretical limit in terms of energy density (~200 Wh/kg) [5]; meanwhile, diesel generators cannot be reduced to mesoscale because of scaling laws governing internal combustion engines [6]. On the other hand, conventional hydrocarbon fuels have higher energy densities of ~12 kWh/kg [6], so that even a relatively inefficient generator can provide more power than batteries, at the mesoscale.

In a TPV system, a heat source heats an emitter to a high temperature, then the emitter emits thermal radiation that is converted to electricity by a photovoltaic cell [7–12]. As shown in Fig. 1a, a TPV system consists of a hot side, with the heat source (in this case a microcombustor) and emitter, and a cold side with the photovoltaic cell. The advantages of TPV are that the conversion is a quiet and static process (there are no moving parts), and unlike thermoelectrics, there is not a need to maintain a temperature gradient and the paths of heat conduction and electricity generation are physically separated.

However, in part because the TPV system includes multiple components, each of which needs to be highly efficient, it is challenging to design high-performance TPV systems.

One way to increase the performance of the TPV system is to use a selective emitter. A selective emitter is one that preferentially emits in-band photons, or photons with energy above or wavelength shorter

* Corresponding author.
E-mail address: reyu@alum.mit.edu (R. Sakakibara).

https://doi.org/10.1016/j.solmat.2021.111536
Received 15 July 2021; Received in revised form 23 October 2021; Accepted 2 December 2021
Available online 13 January 2022

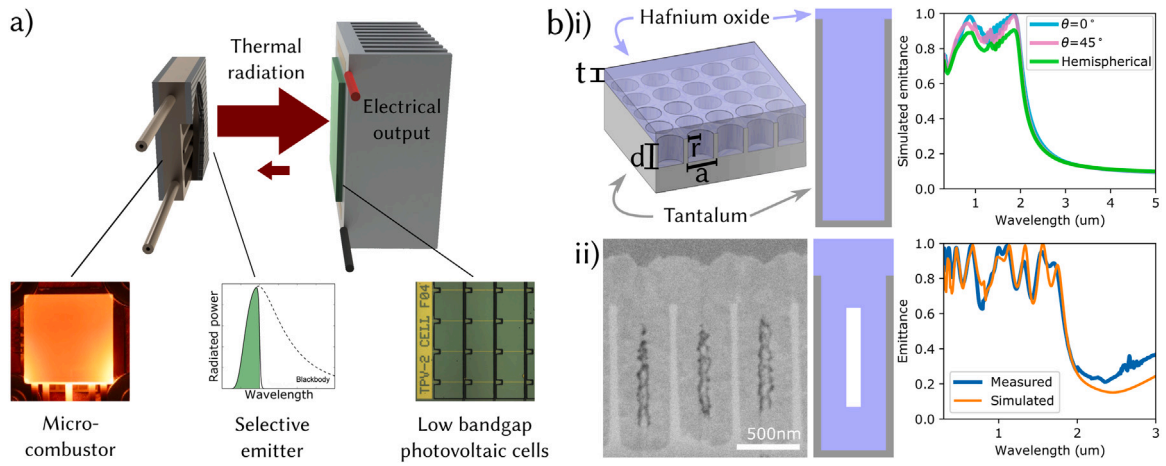

Fig. 1. One way to increase the overall efficiency and power density of a thermophotovoltaic (TPV) system is to use a selective emitter. (a) In a TPV system, a heat source heats up an emitter that emits thermal radiation that is then converted to electricity by a low bandgap photovoltaic cell. In our group we use a microcombustor (for fuel combustion) and a photonic crystal (PhC) broadband selective emitter on the hot side. (b) The metallodielectric "filled" PhC emitter would enable high optical performance over a wide range of angles, but is difficult to fabricate. (i) This PhC is both filled and capped with hafnium oxide (HfO_2), which allows for high in-band (<2 μm cutoff) emittance and low out-of-band (>2 μm cutoff) emittance for both normal (0°) and off-normal (45°) incidence, as well as hemispherical. The parameters a, r, d, t describe the geometry of the PhC, respectively a the period (pitch) of the cavities, r cavity radius, d cavity depth, and t thickness of capping layer above the cavity. (ii) A previous demonstration of this PhC had two major geometric imperfections, a hollow air core and a thick capping layer, that adversely impacted the emittance. Measurement was at 8° angle, room temperature.

than the photovoltaic cell bandgap. At the same time, it suppresses the emission of out-of-band photons, and thus reduces radiative heat losses from the TPV hot side. In particular, a broadband selective emitter enables high radiated power per area and can lead to high overall electrical power.

Several kinds of selective emitters have been developed for TPV [13,14], including naturally selective emitters [15–20] (such as rare earth metal oxides) and engineered emitters, which include metamaterials [21–28], one-dimensional multilayer aperiodic stacks [29,30], and photonic crystals of one [31–33], two [1,34,35], and three dimensions [36–40].

One type of broadband selective emitter is two-dimensional photonic crystals (PhCs), one type of which is square [41,42] or cylindrical holes [43–46] etched into refractory metal substrates (often tungsten or tantalum). The emission spectrum can be tailored by changing the dimensions of the cavities.

Our group has developed 2D PhCs with both good optical performance [47] and high temperature stability [1]. These PhCs are made of tantalum and coated with 20-40 nm of hafnium oxide, and were used in a prototype TPV system with a demonstrated 4.4% overall system efficiency [1].

The optical performance of the PhC can be further improved by shrinking the cavity dimensions, then filling and capping the cavities with hafnium oxide (rather than just coating the surfaces) [48,49]. This metallodielectric "filled" PhC has higher overall hemispherical emittance in-band compared to the coated PhC, as will be discussed in the Theory section.

The filled PhC is more difficult to fabricate, however. One major difference between the coated and filled PhCs is that the cavity radius of the filled PhC is about half that of the coated PhC. The refractive index of the hafnium oxide (HfO_2) is about 1.9–2, which leads to a smaller cavity radius for the same target optical wavelength. With a smaller cavity radius, the cavities have a higher sensitivity to slight variations in dimensions, as well as higher aspect ratios, which makes them harder to etch and fill.

Our group's first filled PhC [3] had two major geometric imperfections: the cavity was not fully filled with HfO_2 (using atomic layer deposition), and the capping layer was both thick and uneven [4], as shown in the scanning electron microscopy (SEM) image of the cross section (see Fig. 1b-ii, left), which was prepared through focused ion beam (FIB) milling. Both of these imperfections impact the PhC reflectance, as shown in simulated fits to the measured spectrum (see Fig. 1b-ii, plot on the right) [4].

Thus, the PhC must have both a better-filled cavity and a thin capping layer to realize the full theoretical performance of the filled PhC.

Here, we present the fabrication of a filled PhC with close to its full theoretical performance. We present a fabrication process to realize both critical features, the better-filled cavity and thin capping layer. By analyzing fabricated samples using a combination of simulations and SEM cross sections, we identified geometric imperfections that adversely impact the emittance, and others that are minor. In particular we found that (1) the cavity does not need to be completely filled, as long as the hollow core is very thin (2) the capping layer does not need to be perfectly flat and (3) HfO_2 must not be removed from within the cavity.

2. Theory

2.1. Metallic PhC (parameters a, r, d)

To understand PhC emissivity, one can start by considering a single cylindrical metallic cavity (unfilled) within the 2D array.

The intuition is that light can interact with the cavity only if the optical wavelength is smaller than the physical cavity. The cavity radius r sets a cutoff wavelength, which is approximately give by the fundamental cavity resonance [43,48]. At wavelengths shorter than the cutoff, light is able to interact with the cavity, leading to increased interaction times. This leads to an enhanced (in-band) emissivity compared to a flat substrate. Meanwhile, at longer wavelengths, the emissivity remains low [42,43,50]. A sharp transition from high to low emissivity can be observed.

For a particular choice of cavity radius r there is an optimal cavity depth d, as according to coupled-mode theory [51]. There is one cavity depth d that satisfies the Q-matching condition, which occurs when the radiative and absorptive quality factors of the cavity resonances are matched.

The period a is generally set to be small, as it determines the onset of diffraction. Diffraction reduces the in-band emissivity and is especially pronounced at high angles of incidence [48,49]. For the polar angle $\theta = 0°$, the onset of diffraction begins at wavelength shorter than the period, or $\lambda < a$.

2.2. Metallo-dielectric "filled" PhC (parameter t)

It is possible to reduce diffraction losses by filling and capping the cavities with a material with high index of refraction and shrinking the cavity dimensions [48,49]. Filling the cavities allows for the cavity dimensions to be reduced without changing the optical wavelengths.

Hafnium oxide (HfO_2) is chosen as the dielectric material for cavity filling for several reasons: it has a high index of refraction, is transparent in the visible and infrared regions, can be deposited using atomic layer deposition, and is stable at high temperatures [49]. HfO_2 has been used as a protective coating for several TPV emitters, including 3D PhCs [39,40], 1D periodic stacks [30,52], metamaterials [28,53], and our group's previous-generation PhCs that were coated with 20-40 nm of HfO_2 [47,54].

In this design, the PhC is also capped with a layer of HfO_2, whose thickness is given by the parameter t. The capping layer of HfO_2 gives rise to a resonance peak whose position depends on the thickness; it acts similarly to an anti-reflective coating. When this capping layer is thick, the corresponding resonance peak is out-of-band.

A 3D schematic of this PhC is shown in the left side of Fig. 1b-i, labeled with the parameters a, r, d, and t.

2.3. Calculation of (intermediate) optical metrics

We used four different optical metrics (both relative and absolute metrics) as intermediate metrics for overall system output power per area. The four metrics are as follows:

- In-band radiated power per area, calculated as

$$\pi \int_0^{\lambda_c} \varepsilon(\lambda,T)|_{\theta=8^\circ} I_b(\lambda,T) d\lambda \tag{1}$$

- Out-of-band radiated power per area, calculated as

$$\pi \int_{\lambda_c}^{\infty} \varepsilon(\lambda,T)|_{\theta=8^\circ} I_b(\lambda,T) d\lambda \tag{2}$$

- Spectral selectivity, calculated as

$$\frac{\int_0^{\lambda_c} \varepsilon(\lambda,T)|_{\theta=8^\circ} I_b(\lambda,T) d\lambda}{\int_0^{\infty} \varepsilon(\lambda,T)|_{\theta=8^\circ} I_b(\lambda,T) d\lambda} \tag{3}$$

- Deviation of the emittance spectrum from a step function, where the sum of square error is normalized to the number of sampled points N

$$\frac{1}{N}\sum^{N}(\text{measured}(\lambda) - \text{step function}(\lambda))^2 \tag{4}$$

where λ is wavelength, λ_c is the cutoff wavelength, which often corresponds to the photovoltaic (PV) cell band-gap, T is temperature (we calculate for 1000 °C), $\varepsilon(\lambda,T)|_{\theta=8^\circ}$ is the emittance (at room temperature and at near-normal angle 8°; since these are only intermediate metrics we do not approximate or use the hemispherical emittance), $I_b(\lambda,T)$ is the blackbody intensity from Planck's law:

$$I_b(\lambda,T) = \frac{2hc^2}{\lambda^5}\frac{1}{e^{hc/\lambda k_B T} - 1} \tag{5}$$

We seek to simultaneously increase the in-band radiated power per area and spectral selectivity and decrease the out-of-band radiated power per area and deviation from step function.

3. Simulations

3.1. Simulations of PhC emittance with S^4

For our simulations, including fits to measured spectra, we use S^4 (Stanford Stratified Structure Solver), an electromagnetics solver for layered periodic structures that uses rigorous coupled wave analysis (RCWA) methods [55]. Tantalum dispersion parameters are based on a Lorentz-Drude model fit to the measured reflectance of flat tantalum wafers. The index of refraction of HfO_2 is set to 2, which is consistent with our measurements of flat HfO_2 and close to reported values in the literature [56].

The four major parameters of a typical filled PhC are the period a, radius r, depth d, and thickness of HfO_2 capping layer t, as discussed in Section 2.

3.2. Building photonic crystal models in S^4

Generally, we can account for the geometric imperfections of realistic PhCs in our S^4 models. We introduce geometric imperfections into the models by modifying the layered structure, and adding additional geometric variables. The layers in S^4 are discrete with finite dimensions (thickness and radius). In the case of rounded, non-straight features (like the bowl-shape described later), the feature is discretized into 5–10 layers.

3.3. Fits to experimental spectra

The procedure for finding the best fit to the experimental measurement is as follows: (a) image the photonic crystal cross section, which provides both information about geometric imperfections, if any, and dimensions, (b) build the PhC model in S^4, and (c) use the dimensions measured in (a) as initial guesses for the model parameters.

The fit to a measured spectrum involves minimizing the sum of the square error $\sum(\text{measured}(\lambda) - \text{simulated}(\lambda))^2$, using the Sequential Least Squares Programming (SLSQP) method. Constraints include $a > 2r - 0.1\,\mu m$; typical bounds are $0.1 < a < 1$, $0.1 < r < 1$, $0.1 < d < 10$, $0.02 < t < 1$ (in μm).

3.4. Approximation of hemispherical emittance

In order to calculate the impact of our emitter on a full TPV system, we approximate the hemispherical emittance, which is based on our measurements of near-normal reflectance (at room temperature and at 8° angle).

The hemispherical emittance $\varepsilon'(\lambda,T)$ can be calculated as follows [57]:

$$\varepsilon'(\lambda,T) = \frac{1}{\pi}\int_0^{2\pi}\int_0^{\pi/2} \varepsilon(\lambda,T,\theta,\phi)\cos\theta\sin\theta d\theta d\phi \tag{6}$$

To go from near-normal reflectance to hemispherical emittance we first (a) calculate the near-normal 8°, room-temperature emissivity: 1 - measured reflectance, then (b) use S^4 to find the photonic crystal geometry that best fits the measured emittance (see Simulations Section 3.3).

Once the best-fit photonic crystal geometry is determined, we simulate this structure at thirty-nine angles (θ, ϕ). These angles (θ, ϕ) correspond to equivalently-spaced points [58] that lie on one sixteenth of a sphere (or one eighth of a hemisphere). Because the PhC has symmetry in the ϕ plane, we do not need to integrate over the entire hemisphere.

Then we integrate as follows:

$$\varepsilon'(\lambda,T) = \frac{8}{\pi}\int_0^{\pi/4}\int_0^{\pi/2} \varepsilon(\lambda,T,\theta,\phi)\cos\theta\sin\theta d\theta d\phi \tag{7}$$

3.5. System-level modeling

We estimate the system output power based on the prototype TPV system from a previous paper from our group [1], which used a tantalum PHC that was only coated (not filled and capped) with HfO_2. In this TPV system, 100 W of propane combustion with oxygen led to 4.4 W of electrical power, using InGaAs cells with cutoff 2 μm and a previous-generation coated PhC.

In our calculations we use almost all the same parameters as this system, except we varied the emitter (therefore its spectrum).

The model (described in more detail in [6,59]) is based on a fuel-based (combustion-based) TPV system. The microburner is two-sided, with two planar emitters in thermal contact; a planar cell faces and is separated from each emitter by about 1 mm.

The model includes three parts: thermal, optical, and electrical. First, in the thermal model, the final temperature of the hot side and thus the emitter are calculated, as well as the flux out of the emitter; then in the optical model the view factor and the radiation incident on the photovoltaic cell, are calculated; then in the electrical model, a current–voltage curve is calculated using an equivalent circuit model for the photovoltaic cell.

The combustion of propane occurs as follows:

$$C_3H_8 + 5O_2 \longrightarrow 3CO_2 + 4H_2O \tag{8}$$

The thermal model involves a heat balance equation:

$$Q_{comb} = Q_{exh} + Q_{side} + Q_{cond} + Q_{emit} \tag{9}$$

where Q_{comb} is the heat of combustion in W, Q_{exh} is the exhaust heat loss (where excess oxygen exists, this is heated as well), Q_{side} is radiation from the sides of the microburner, Q_{cond} is the conduction heat loss from the tubes of the microburner, and Q_{emit} is the net heat flux emitted by the emitter (though it is not necessarily described by Planck's law and the emittance, because of reflections that can occur at the cell). The hot side temperature T_b (thus the temperature of the emitter) is determined from this heat balance equation.

In the optical model, the emitter and the cell each form one end of a cavity. With detailed balance, the net flux out of the emitter ($q_{e,\,\mathrm{out}} - q_{e,\,\mathrm{in}}$) can be expressed as follows, in terms of the emitter area A_e, the view factor F, reflectivity of cell $\rho_c(\lambda)$, reflectivity of emitter $\rho_e(\lambda)$, emissivity of emitter ε_e, wavelength λ, and temperature of hot side T_b:

$$q_{e,\,\mathrm{out}} - q_{e,\,\mathrm{in}} = A_e \pi \int_0^\infty \frac{1 - F^2\rho_c(\lambda)}{1 - F^2\rho_c(\lambda)\rho_e(\lambda)} \varepsilon_e(\lambda) I_b(\lambda, T_b) d\lambda \tag{10}$$

The view factor F is approximated by two coaxial disks (the cell and emitter each have area 20 mm x 20 mm) separated by a distance of 1 mm [57]. Its numerical value is about 0.96.

In the electrical model, radiation incident on the cell is converted into electrical power output in two steps: (a) incident light is converted into photocurrent, using the empirical external quantum efficiency (EQE) of the InGaAs cell, and (b) an equivalent circuit model is used to generate a current–voltage curve, from which the maximum power point can be extracted.

The radiation incident on the cell is:

$$q_{c,\mathrm{in}} = A_e \pi \int_0^\infty \frac{F}{1 - F^2\rho_c(\lambda)\rho_e(\lambda)} \varepsilon_e(\lambda) I_b(\lambda, T_b) d\lambda \tag{11}$$

where $q_{c,\mathrm{in}}$ is the flux out of the emitter $q_{e,\mathrm{out}}$ multiplied by the view factor F.

The photocurrent I_{ph} is:

$$I_{ph} = e \int_0^\infty \frac{\lambda}{hc} q_{c,\mathrm{in}}(\lambda) \mathrm{EQE}(\lambda) d\lambda \tag{12}$$

where hc/λ is the photon energy and e electron charge.

The equivalent circuit is:

$$I = I_{ph} - I_0 \left(\exp\left[\frac{q}{n k_B T_j} (V + I R_s) \right] - 1 \right) - \frac{V + I R_s}{R_{sh}} \tag{13}$$

where I and V are the terminal current and voltage, $q/k_B T_j$ is the thermal voltage, I_0 is the diode dark current, n is the diode ideality factor, and R_s and R_{sh} are the shunt and series resistances.

The equivalent circuit parameters and EQE were extracted from experimental data [59].

The electrical power output was taken at the maximum power point.

4. Material and methods

4.1. Fabrication of metallic cavities

The fabrication of the metallic cavities is almost identical to that described elsewhere (for PhCs from our group) [3]: (1) generate a pattern using interference lithography, with a trilayer resist (resist, SiO_2 adhesion layer, anti-reflection coating ARC) (2) enlarge the cavity diameter with isotropic plasma ashing (3) pattern transfer through the resist stack (CF_4 for SiO_2 adhesion layer, He + O_2 for ARC) with reactive ion etching (RIE) (4) pattern transfer into a SiO_2 hard mask with CHF_3 + CF_4 RIE. (5) For the final etching of the tantalum substrate we used a Bosch etch process using SF_6 and C_4F_8 [3].

4.2. Cavity filling

To deposit HfO_2 via ALD, we used a thermal ALD system (Veeco/Cambridge Nanotech Savannah S200), with precursors Tetrakis-(dimethylamido) -hafnium and water, at 65 °C, with flow of 5 sccm. The deposition temperature was set to 190 °C.

One difficulty with filling the cavities is that the cavities have high aspect ratios: diameter of ~400 nm and depth of 1.3-2 μm (deeper, around 4-5 μm, is better but we target lower depths to make the fabrication easier).

While with ALD the HfO_2 can be deposited layer by layer, in practice our PhC cavities were not completely filled and a hollow air core developed within.

To address the issue of cavity filling, we used exposure mode ALD instead, where for each cycle, extra time of 10 s is given for each precursor to diffuse into the cavities [60].

4.3. Room temperature reflectance measurements

We measure the PhC reflectance at room temperature, over a spot size of about 5 mm in diameter, using a UV-vis spectrophotometer. For calibration we use four points: a high reflectance standard, beamsplitter with intermediate reflectance, low reflectance standard, and blocked beam. We measure normal at 8° and off-normal at 45°.

4.4. Focused ion beam milling

To image the PhC cross sections, we first deposit platinum or both carbon and platinum on the top surface of the sample, then mill using gallium ions. All cross section images show approximately the center of each cavity, where the tantalum sidewalls are the thinnest. Curtaining imaging artifacts are especially pronounced where the cavity has a hollow air core, and at the cavity sidewalls.

4.5. Control of hafnium oxide capping layer

For etching, we used an argon ion milling process (physical dry etch) with argon flow 200 sccm, source power 500 W, substrate power 150 W, pressure about 1 mT, and substrate temperature 20 °C.

The spin-on glass we used was Filmtronics Silicates 15 A. We spuncoat the spin-on glass as follows: spin at 3000 rpm, prebake at ~80 °C for 60 s and at 200 °C for 60 s, then spin another layer (for a total of two layers). We annealed at 475 °C, with a ramp of 5 °C/min and hold of 1 h, under vacuum of $\sim 1 \times 10^{-6}$ mbar in a quartz tube furnace.

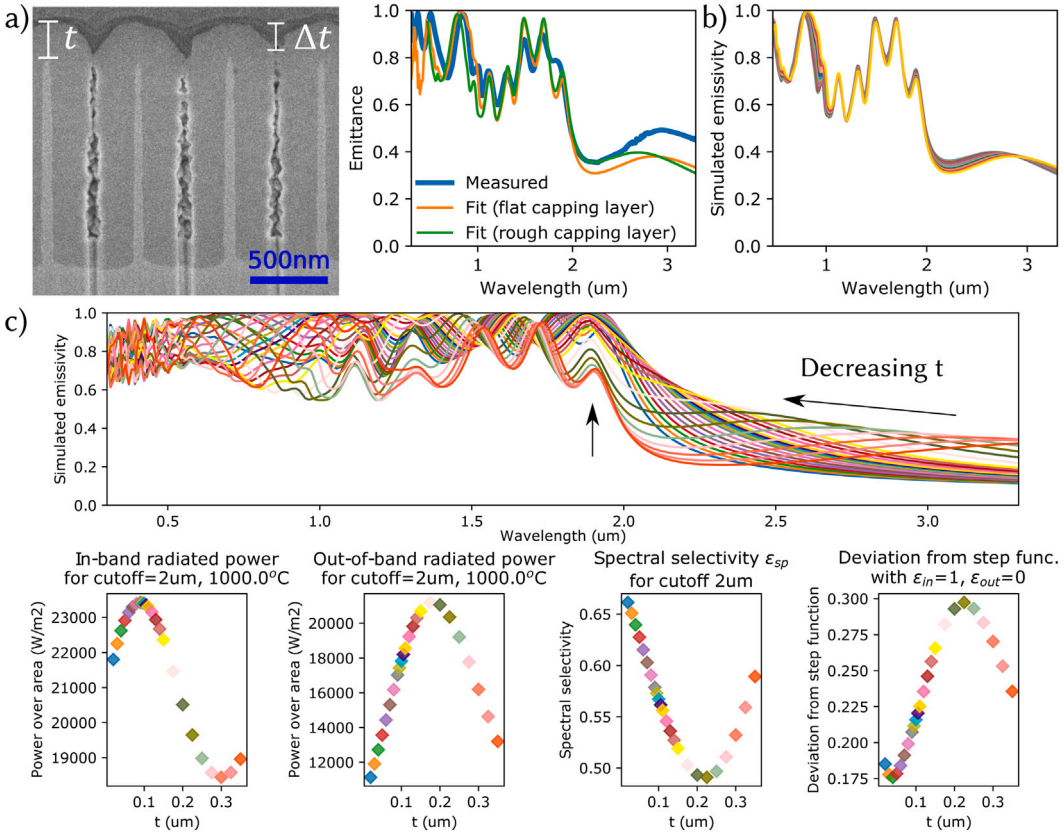

Fig. 2. Filling the cavities more fully leads to a thick and uneven capping layer, whose thickness must be controlled (reduced) for good optical performance. (a) The benefit of exposure mode atomic layer deposition is that it more fully fills the cavity (the thin air core does not impact the emittance); however, it leads to a thick and uneven capping layer with 160-200 nm height difference (the difference is labeled as Δt), with the thickest part (labeled t) about 270 nm. We can model this PhC as if it has a flat capping layer, however. The critical parameter is the thickness of the thickest part of the capping layer, t. (b) We also modeled PhCs with uneven capping layers, keeping the thickest part the same but varying the unevenness. Unevenness has a minor impact on the emittance. (c) The emittance and the four metrics improve as t decreases (range of t 20-350 nm). As t decreases, there are two effects on the emittance spectrum: (1) the out-of-band resonance peak blue-shifts and eventually disappears (2) the in-band resonance peak increases in absolute emittance. The thickness t should be less than 110 nm, but the optimal t changes depending on system-level parameters. (For interpretation of the references to color in this figure legend, the reader is referred to the web version of this article.)

4.6. High-temperature anneal of photonic crystal

We annealed the photonic crystal sample for 100 h at 1000 °C under vacuum of $\sim 1 \times 10^{-6}$ mbar. The sample was annealed in a quartz tube furnace, with a temperature ramp as follows: (a) ramp from room temperature to 275 °C at 5 °C min^{-1}, (b) hold at 275 °C for 1 h (to off-gas moisture), (c) ramp from 275 to 1000 °C at 5 °C min^{-1}, (d) hold at 1000 °C for 100 h, (e) let cool naturally.

We chose the temperature 1000 °C to be consistent with previous annealing experiments on our group's first filled PhC (24 h at 1000 °C [3]).

5. Results and discussion

5.1. Analysis of PhC filled with exposure mode ALD

5.1.1. Characterization

After filling the tantalum cavities with HfO_2 using exposure mode ALD, we imaged the PhC cross section and measured its room temperature reflectance. As shown in Fig. 2a, the cavity is characterized by (1) a thin hollow air core inside and (2) a capping layer that is both thick and uneven.

However, from our simulated fits (Fig. 2a) we found that (1) the hollow air core no longer has an effect on the reflectance, likely because it is very thin, and (2) the critical parameter is the thickness of the thickest part of the capping layer. Although the PhC has an uneven capping layer, it can be modeled as if it had a flat capping layer (orange curve in Fig. 2a).

The unevenness has a minor impact on the emittance. Fig. 2b shows (overlaid, in different colors) simulated emittance spectra of PhCs with uneven capping layers, where the thickness part is kept constant at $t_{\text{thickest-area}} = 273$ nm but the thinnest part is varied. The yellow spectrum on top shows the spectrum of the PhC with the flat capping layer. A few observations can be made: (1) the off-band resonance peak blue-shifts as $\Delta t = t_{\text{thickest-area}} - t_{\text{thinnest-area}}$ increases, which makes sense because the overall thickness of the capping layer decreases (since the thinnest part of the capping layer is becoming thinner, while the thickest part remains the same, the capping layer overall is becoming thinner as well), (2) for the in-band resonance peaks from 1-2 μm, the position does not change but the absolute emittance appears to slightly increase as Δt increases (it is not clear why).

It appears, therefore, that the PhC capping layer need not be completely flat.

5.1.2. Simulations of varying t

The critical parameter that must be controlled is the thickest part of the capping layer. We simulated PhCs of varying thicknesses ranging from 20 nm to 350 nm (using a model with flat capping layer), the results of which are shown in Fig. 2c. We found that as t decreases, (1) the absolute emittance of the in-band resonance peak closest to the cutoff (~1.9 μm) increases and (2) the out-of-band resonance peak blue shifts and the transition from high to low emittance becomes increasingly sharper.

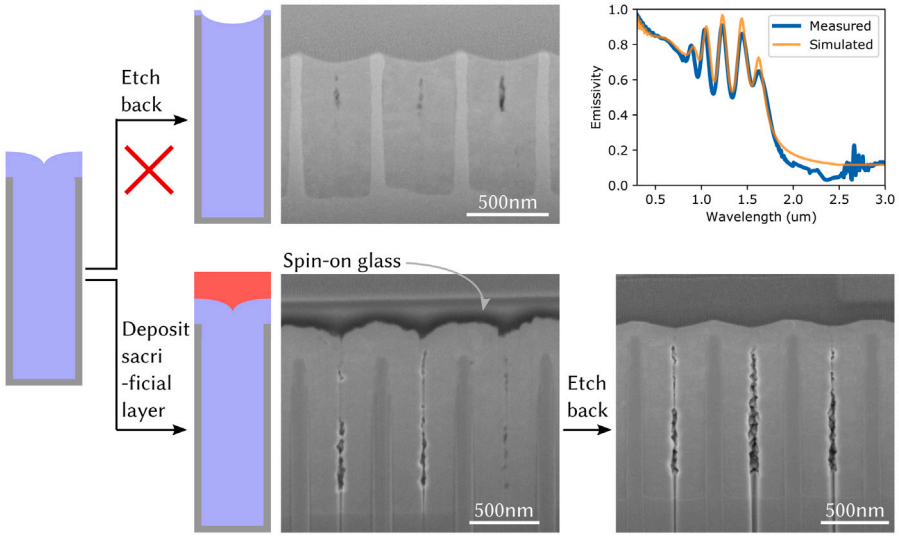

Fig. 3. Planarization and etch back works for reducing both the capping layer thickness and unevenness. The approach of simply etching (top) removes HfO_2 from within the cavity, as shown in the cross section, and this HfO_2 removal reduces the in-band emittance. The other approach (bottom) of planarization and etch back involves first depositing spin-on glass. The cross section after spin-on glass deposition shows that spin-on glass conforms to the HfO_2 top surface, and the top surface of the spin-on glass itself is flat. (The black halo in the spin-on glass is due to charging.) After etch back, the HfO_2 capping layer is thinner and less uneven.

We also plotted the impact of varying t (20-350 nm) on the four optical metrics (Fig. 2c). We find that there is no monotonic trend in the metrics. Starting at 350 nm, the metrics become worse (decrease for in-band radiated power per area and spectral selectivity, increase for out-of-band radiated power and deviation from step function) before getting better. The thickness t at which the best value of each metric occurs depends on the metric.

For our TPV system our optimal range of t is 20-90 nm. It is important to increase the in-band radiated power per area, while simultaneously reducing the out-of-band radiated power per area. While the in-band radiated power per area is highest at 90 nm and decreases as t becomes smaller, out-of-band radiated power per area also decreases as t decreases. The relative impacts of the decrease in in-band as opposed to decrease in out-of-band radiated power per area ultimately depends on system configuration.

5.2. Two approaches to reduce the capping layer thickness

We took two approaches to try to reduce the capping layer thickness, (1) simply etch the capping layer and (2) flatten the capping layer before etching, with the latter ultimately successful. We used a physical etch process: argon ion milling.

The first approach of simply etching the sample did not work because it resulted in HfO_2 being removed from within the cavity (shown in the top part of Fig. 3). This is clear in the cross section image: in particular, the HfO_2 is recessed within the cavity, with a slightly curved surface. Based on this, we made a geometric model in S^4 with a "bowl"-like shape in the HfO_2 (the bowl has a parabolic shape, and is discretized into in six layers in S^4). This model describes well the measured emittance spectrum.

For the second approach, we first planarized the sample by depositing a sacrificial layer. We used spin-on glass, which can be spuncoat and prebaked, then annealed at 475 °C to form an SiO_2-like cross-linked oxide material. We confirmed the planarization by imaging the cross section (left bottom of Fig. 3): the layer directly above the HfO_2 capping layer is spin-on glass. The spin-on glass conforms to the HfO_2 capping layer on the bottom, while its top surface is planar. The black halo appears due to the spin-on glass charging in the SEM.

After planarizing and then etching the sample, the HfO_2 capping layer was both thinner and less uneven. We imaged the resulting cross section, shown in the bottom right of Fig. 3. Before planarization and etch back, the thickness (of the thickest part) of the capping layer t was about 270 nm with a difference Δt between the thickest and thinnest parts of the capping layer about 160-200 nm. Afterwards, the thickness t is about 170 nm, with a Δt of about 70 nm.

5.3. Monitoring the progression of emittance and optical metrics

After doing one pass of planarization and etch back, we continued etching the sample (but without any further planarization, as after the first pass the capping layer was flat enough).

As we etched the sample we monitored the emittance, as well as the corresponding optical metrics. This progression is shown in Fig. 4, which includes the PhC just after filling (in green, with t = 273 nm) and the PhC after one pass of planarization and etch back (in red). The subsequent etches are shown as gray, brown, and purple curves. The lines correspond to average emittance, and shading to confidence intervals.

The emittance changed as we etched the sample (and therefore the capping layer thickness decreased), which is as expected from the simulations. Two changes were observed: (a) the absolute value of the in-band resonance peak around 1.8 μm increased, and (b) the out-of-band resonance peak blue-shifted and eventually disappeared.

As the emittance changed, so did the four optical metrics, which generally improved as the sample was etched. As the sample was etched and the thickness decreased, the in-band radiated power per area and spectral selectivity increased, while out-of-band radiated power and the deviation from the step function decreased. The trend of each metric follows the pattern expected from the simulations, which is shown in Fig. 2.

5.4. Characterization of final PhC and system performance estimates

We confirmed that the PhC had the desired near-normal and off-normal emittance and the expected structure. We measured the final PhC's room-temperature reflectance at θ = 8° and 45°, and imaged the cross section, as shown in Fig. 5a–b. As suggested by simulations, the in-band emittance is high for both θ = 8° and 45°, and thus lead to a higher hemispherical emittance. The thickness of the capping layer in the cross section image is around 50 to 60 nm, which is reasonably consistent with the thickness from our simulated fit, 69 nm.

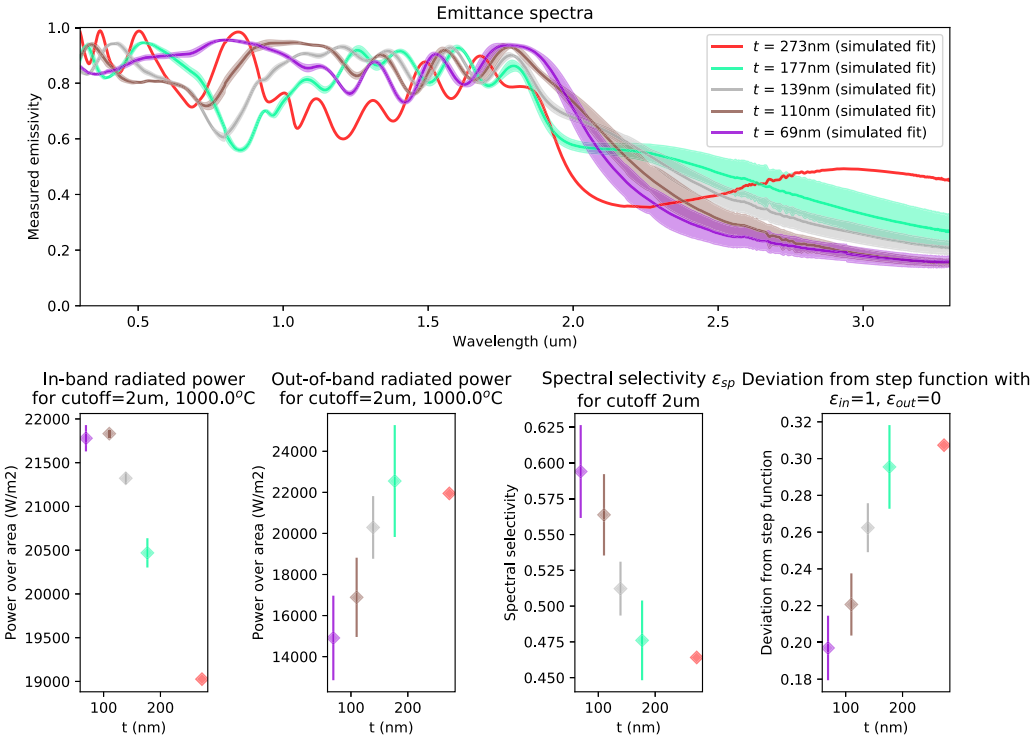

Fig. 4. The emittance and metrics of the PhC do generally improve as the sample is progressively etched and the capping layer thickness decreases. Initially, just after cavity filling, the PhC has a thick capping layer of ~270 nm; the spectrum of this PhC and metrics are indicated by the red curve and dots. Then, after one pass of planarization and etch back, the PhC capping layer thickness is closer to 180 nm (green). The rest of the curves (gray, brown, purple) show the spectrum of the PhC as it is etched further (and thus the capping layer becomes thinner). At t about 70 nm (purple curve), the emittance spectrum shows a sharp transition between high in-band emittance and low out-of-band emittance. Shading in the top plot, and lines in the bottom plots indicate confidence intervals. Note that the bottom plots are shown as a function of thickness t (and not in the chronological order in which the sample was etched). (For interpretation of the references to color in this figure legend, the reader is referred to the web version of this article.)

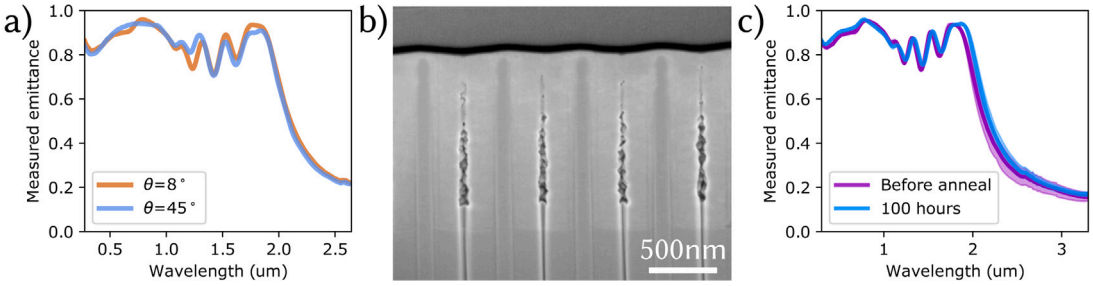

Fig. 5. The fabricated PhC has an overall higher in-band emittance over a wide range of angles, enabling up to an estimated 37.5% increase in system power. (a) Emittance spectra at 8° and 45° for the same region on the sample are similar. (b) Cross section images show a thin (but not completely flat) capping layer, with about 50-60 nm thickness. (c) There is no observable degradation after the sample was annealed for 100 h at 1000 °C under vacuum of $\sim 1 \times 10^{-6}$ mbar. The measurement was taken at 8° angle and room temperature.

We performed initial tests of high-temperature stability on this PhC by annealing it under vacuum at 1000 °C. After 100 h of continuous annealing, we measured the PhC emittance (at room temperature and at 8° angle), and compared it to the emittance before any annealing (Fig. 5c). Even after annealing at 100 h, there is no observable degradation in the PhC emittance spectrum.

We also estimated the system performance of our final filled PhC, and compared it to that of three other emitters, shown in Fig. 6. In our calculations we varied only the emitter (thus its spectrum), while keeping the other parameters the same, and we compared the system-level performance of four emitters: (1) the conformal (coated) PhC of the original system, in black, (2) the perfect filled PhC optimized in [49] and shown in Fig. 1b-i, in green, (3) the filled PhC with $t \sim$ 273 nm shown in Figs. 2 and 4 in red, in red, and (4) the final filled PhC, with $t = 69$ nm, after planarization and etch back. These emittance spectra have been simulated (at room temperature) to take account of long-wavelength radiation, and in particular, for PhCs 1, 2, and 4, we have used the hemispherical emittance. (Because filled PhC 2 was at an intermediate fabrication stage, we used its spectrum simulated at $\theta = 8°$.) We compare room temperature emittance; the experimental points (black) correspond to a system demonstration using that the emitter that has the room temperature emittance depicted as the black curve in Fig. 6a. At high temperatures, it is expected that the emittance peaks become less sharp, and the out-of-band emittance increases from 0.1–0.2 to about 0.3–0.4.

Compared to the previous conformal PhC (black curve, Fig. 6), the filled PhCs (green, purple, red curves) have higher in-band (hemispherical) emittance. However, the filled PhC with a thick capping layer $t =$ 273 nm also has high out-of-band (long-wavelength) emittance.

The system with our final PhC gives an estimated power output as high as 6.0 W, up to a 37.5% increase over the measured 4.4 W power output from the original system. Interestingly, the system using the PhC with the thick capping layer (red) has a comparable power output to the original system. Even though the PhC with the thick capping layer has

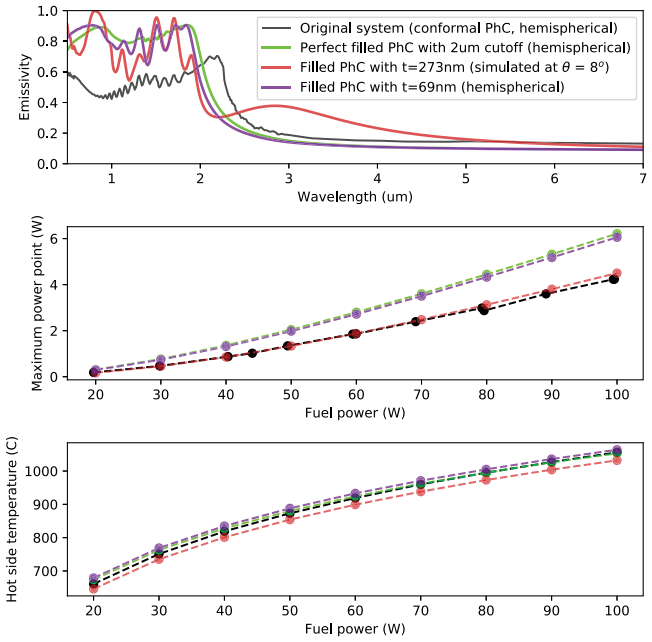

Fig. 6. Comparison of experimental data from a previous prototype system demonstration with a conformal PhC, with system-level simulations of three filled PhCs (the perfect simulated PhC (shown in Fig. 1b-i), the PhC with the thick capping layer, the PhC after planarization and etch back with capping layer about 70 nm). Top: comparison of emittance spectra of different PhCs. Overall, the filled PhCs have higher in-band (hemispherical) emittance compared to the conformal PhC (black), but the filled PhC with thick capping layer (red) also has high out-of-band emittance. Middle: The previous system demonstration yielded 4.4 W for 100 W input. The fabricated PhC with the thin capping layer (purple) yields an estimated system output power as high as 6.0 W, approaching the estimated performance of the perfect PhC (6.2 W yield). Bottom: at fuel input power of 100 W, the hot side temperature (and thus the emitter) gets to about 1060 °C. (For interpretation of the references to color in this figure legend, the reader is referred to the web version of this article.)

high in-band emittance, it appears that the high out-of-band emittance leads to losses and thus reduced overall output power, at least for this system configuration.

Finally, at input fuel power of 100 W, the simulated hot side temperature is about 1060 °C; since experimentally our PhC appears stable for at least 100 h at 1000 °C, we can expect that the PhC can be reasonably robust under such system conditions.

6. Conclusions

We have realized a metallodielectric “filled" PhC with high optical performance at both normal and off-normal incidence, with a sharp cutoff at 2 μm. In order to do this, we developed a fabrication process that enabled us to control both the cavity filling and the capping layer thickness, two parameters that we identified are critical to this PhC design.

While this PhC’s high-temperature stability is not yet determined, this PhC represents a significant improvement over our previous PhC designs, and we have estimated up to a 37.5% increase in system output.

Declaration of competing interest

The authors declare that they have no known competing financial interests or personal relationships that could have appeared to influence the work reported in this paper.

Acknowledgments

The authors would like to thank: Jun Yan of UNC Chapel Hill, James Daley of MIT for fabrication assistance with the photonic crystal; Mark Mondol and Ian Christen of MIT, and Scott Wheelock, Ben Burtner, and Seth Burtner of Filmtronics, Inc. for assistance with planarization and spin-on glass troubleshooting; Timothy McClure and Gary Riggott of MIT for assistance with reflectance measurements.

This work was supported by the Army Research Office, United States through the Institute for Soldier Nanotechnologies under Award No. W911NF-13-D-0001 and W911NF-18-2-0048.

This work was performed in part at the NanoStructures Laboratory (NSL) at MIT; the Chapel Hill Analytical and Nanofabrication Laboratory, CHANL, a member of the North Carolina Research Triangle Nanotechnology Network, RTNN, which is supported by the National Science Foundation, United States, Grant ECCS-2025064, as part of the National Nanotechnology Coordinated Infrastructure, NNCI; and the Harvard University Center for Nanoscale Systems (CNS), a member of the National Nanotechnology Coordinated Infrastructure Network (NNCI), which is supported by the National Science Foundation, United States under NSF award no. ECCS-2025158. Veronika Stelmakh and Walker Chan are co-founders of Mesodyne, Inc.

References

[1] W.R. Chan, V. Stelmakh, M. Ghebrebrhan, M. Soljačić, J.D. Joannopoulos, I. Čelanović, Enabling efficient heat-to-electricity generation at the mesoscale, Energy Environ. Sci. 10 (2017) 1367.

[2] V. Stelmakh, A Practical High Temperature Photonic Crystal for High Temperature Thermophotovoltaics, (Ph.D. thesis), Massachusetts Institute of Technology, 2017.

[3] V. Stelmakh, W.R. Chan, M. Ghebrebrhan, M. Soljačić, J.D. Joannopoulos, I. Čelanović, Fabrication of an omnidirectional 2D photonic crystal emitter for thermophotovoltaics, J. Phys.: Conf. Ser. 773 (2016) 012037.

[4] R. Sakakibara, V. Stelmakh, W.R. Chan, M. Ghebrebrhan, J.D. Joannopoulos, M. Soljačić, I. Čelanović, Improved omnidirectional 2D photonic crystal selective emitter for thermophotovoltaics, J. Phys.: Conf. Ser. 1052 (2018).

[5] C.-X. Zu, H. Li, Thermodynamic analysis on energy densitites of batteries, Energy Environ. Sci. 4 (2011) 2614–2624.

[6] W.R. Chan, High Efficiency Thermophotovoltaic Microgenerators, (Ph.D. thesis), Massachusetts Institute of Technology, 2015.

[7] E. Doyle, K. Shukla, C. Metcalfe, Development and Demonstration of a 25 Watt Thermophotovoltaic Power Source for a Hybrid Power System, Tech. rep. tr04-2001, National Aeronautics and Space Administration, 2001.

[8] L. Fraas, J. Avery, L. Minkin, J. Strauch, Design and Thermal Modeling of a Portable Fuel Fired Cylindrical TPV Battery Replacement, Technical report, Sandia National Laboratories, 2010.

[9] B. Bitnar, W. Durisch, R. Holzner, Thermophotovoltaics on the move to applications, Appl. Energy 105 (2013) 430–438.

[10] T. Burger, C. Sempere, B. Roy-Lainde, A. Lenert, Present efficiencies and future opportunities in thermophotovoltaics, Joule 4 (8) (2020) 1660–1680.

[11] N. Horiuchi, Efficient thermophotovoltaics, Nat. Photon. (2020).

[12] M. Suemitsu, T. Asano, T. Inoue, S. Noda, High-efficiency thermophotovoltaic system that employs an emitter based on a silicon rod-type photonic crystal, ACS Photonics 7 (1) (2020) 80–87.

[13] N.A. Pfiester, T.E. Vandervelde, Selective emitters for thermophotovoltaic applications, Phys. Status. Solidi A 214 (1) (2017).

[14] R. Sakakibara, V. Stelmakh, W.R. Chan, M. Ghebrebrhan, J.D. Joannopoulos, M. Soljačić, I. Čelanović, Practical emitters for thermophotovoltaics: A review, J. Photonics Energy 9 (3) (2019) 032713.

[15] K.W. Stone, D.L. Chubb, D.M. Wilt, M.W. Wanlass, Testing and modeling of a solar thermophotovoltaic power system, AIP Conf. Proc. 199 (1996) 199–209.

[16] K.C. Chen, D. Osborn, P. Sarmiento, A. Prasad, S. Earath, Small, Efficient Thermophotovoltaic Power Supply, Technical Report DAAG55-97-C-0003, U.S. Army Research Office, 1999.

[17] H. Yugami, H. Sai, K. Nakamura, N. Nakagawa, H. Ohtsubo, Solar thermophotovoltaic using al2o3/Er3Al5O12 eutectic composite selective emitter, IEEE Photovoltaic Spec. Conf. 28 (2000) 1214–1217.

[18] B. Bitnar, W. Durisch, J.-C. Mayor, J. Sigg, H.R. Tschudi, Characterisation of rare earth selective emitters for thermophotovoltaic applications, Sol. Energy Mater. Sol. Cells 73 (2002) 221–234.

[19] S. Bitnar, W. Durisch, G. Palfinger, F. von Roth, U. Vogt, A. Brönstrup, D. Seiler, Practical thermophotovoltaic generators, Semiconductors 28 (2004) 941–945.

[20] R.E. Nelson, Tpv systems and state-of-art development, in: T.J. Coutts, G. Guazzoni, J. Luther (Eds.), Fifth Conference on Thermophotovoltaic Generation of Electricity, in: American Institute of Physics Conference Series, vol. 653, 2003, pp. 3–17.
[21] J. Hao, J. Wang, X. Liu, W.J. Padilla, L. Zhou, M. Qiu, High performance optical absorber based on a plasmonic metamaterial, Appl. Phys. Lett. 96 (2010) 351104.
[22] B. Zhang, J. Hendrickson, J. Guo, Multispectral near-perfect metamaterial absorbers using spatially multiplexed plasmon resonance metal square structures, J. Opt. Soc. Amer. B 30 (2013) 656.
[23] C. Shemelya, D. DeMeo, N. Pfiester Latham, X. Wu, C. Bingham, W. Padilla, T.E. Vandervelde, Stable high temperature metamaterial emitters for thermophotovoltaic applications, Appl. Phys. Lett. 104 (2014) 201113.
[24] W. Li, U. Guler, N. Kinsey, G.V. Naik, A. Boltasseva, J. Guan, V.M. Shalaev, A.V. Kildishev, Refractory plasmonics with titanium nitride: Broadband metamaterial absorber, Adv. Mater. 26 (2014) 7959–7965.
[25] D. Woolf, J. Hensley, J.G. Cederberg, D.T. Bethke, A.D. Grine, E.A. Shaner, Heterogeneous metasurface for high temperature selective emission, Appl. Phys. Lett. 105 (2014) 0181110.
[26] D.N. Woolf, E.A. Kadlec, D. Bethke, A.D. Grine, J.J. Nogan, J.G. Cederberg, D.B. Bruckel, T.S. Luk, E.A. Shaner, J.M. Hensley, High-efficiency thermophotovoltaic energy conversion enabled by a metamaterial selective emitter, Optica 5 (2) (2018) 213–218.
[27] P.N. Dyachenko, S. Molesky, A. Yu Petrov, M. Störmer, T. Krekeler, S. Lang, M. Ritter, Z. Jacob, M. Eich, Controlling thermal emission with refractory epsilon-near-zero metamaterials via topological transitions, Nature Commun. 7 (2016) 11809.
[28] M. Chirumamilla, G.V. Krishnamurthy, K. Knopp, T. Krekeler, M. Graf, D. Jalas, M. Ritter, M. Störmer, A.Y. Petrov, M. Eich, Metamaterial emitter for thermophotovoltaics stable up to 1400 °c, Nat. Sci. Rep. 9 (2019) 7241.
[29] M. Shimizu, A. Kohiyama, J. Yugami, High-efficiency solar-thermophotovoltaic system equipped with a monolithic planar selective absorber/emitter, J. Photon. Energy 5 (2015) 053099.
[30] A. Kohiyama, M. Shimizu, H. Yugami, Unidirectional radiative heat transfer with a spectrally selective planar absorber/emitter for high-efficiency solar thermophotovoltaic systems, Appl. Phys. Express 9 (2016) 112302.
[31] W.R. Chan, P. Bermel, R.C.N. Pilawa-Podgurski, C.H. Marton, K.F. Jensen, J.J. Senkevich, J.D. Joannopoulos, M. Soljačić, I. Čelanović, Toward high-energy-density, high-efficiency, and moderate-temperature chip-scale thermophotovoltaics, Proc. Natl. Acad. Sci. USA 110 (14) (2013) 5309–5314.
[32] A. Lenert, D.M. Bierman, Y. Nam, W.R. Chan, I. Čelanović, M. Soljačić, E.N. Wang, A nanophotonic solar thermophotovoltaic device, Nature Nanotechnol. 9 (2014) 126–130.
[33] D.M. Bierman, A. Lenert, W.R. Chan, B. Bhatia, I. Čelanović, M. Soljačić, E.N. Wang, Enhanced photovoltaic energy conversion using thermally based spectral shaping, Nature Energy 1 (2016).
[34] V. Rinnerbauer, A. Lenert, D.M. Bierman, Y.X. Yeng, W.R. Chan, R.D. Geil, J.J. Senkevich, J.D. Joannopoulos, E.N. Wang, M. Soljačić, I. Čelanović, Metallic photonic crystal absorber-emitter for efficient spectral control in high-temperature solar thermophotovoltaics, Adv. Energy. Mater. (2014).
[35] X. Wang, W.R. Chan, V. Stelmakh, M. Soljačić, J.D. Joannopoulos, I. Čelanović, P.H. Fisher, Prototype of radioisotope thermophotovoltaic system using photonic crystal spectral control, J. Phys.: Conf. Ser. 660 (2015) 012034.
[36] S.Y. Lin, J. Moreno, J.G. Fleming, Three-dimensional photonic-crystal emitter for thermal photovoltaic power generation, Appl. Phys. Lett. 93 (2) (2003) 380.
[37] P. Nagpal, S.E. Hon, A. Stein, D.J. Norris, Efficient low-temperature thermophotovoltaic emitters from metallic photonic crystals, Nano Lett. 8 (10) (2008).
[38] M. Garin, D. Hernández, T. Trifonov, R. Alcubilla, Three-dimensional metallo-dielectric selective thermal emitters with high-temperature stability for thermophotovoltaic applications, Sol. Energy Mater. Sol. Cells 134 (2015) 22–28.
[39] K.A. Arpin, M.D. Losego, P.V. Braun, Electrodeposited 3D tungsten photonic crystals with enhanced thermal stability, Chem. Mater. 23 (2011) 4783–4788.
[40] K.A. Arpin, M.D. Losego, A.N. Cloud, H. Ning, J. Mallek, N.P. Sergeant, L. Zhu, Z. Yu, B. Kalanyan, G.N. Parsons, G.S. Girolami, J.R. Abelson, S. Fan, P.V. Braun, Three-dimensional self-assembled photonic crystals with high temperature stability for thermal emission modification, Nature Commun. 4 (2013).
[41] H. Sai, Y. Kanamori, H. Yugami, High-temperature resistive surface grating for spectral control of thermal radiation, Appl. Phys. Lett. 82 (11) (2003) 1685–1687.
[42] H. Sai, H. Yugami, Thermophotovoltaic generation with selective radiators based on tungsten surface gratings, Appl. Phys. Lett. 85 (2004) 3399.
[43] I. Čelanović, N. Jovanić, J. Kassakian, Two-dimensional tungsten photonic crystals as selective thermal emitters, Appl. Phys. Lett. 92 (2008) 193101.
[44] M. Araghchini, Y.X. Yeng, N. Jovanić, P. Bermel, L.A. Kolodziejski, M. Soljačić, I. Čelanović, J.D. Joannopoulos, Fabrication of two-dimensional tungsten photonic crystals for high-temperature applications, J. Vac. Sci. Technol. B 29 (2011) 61402.
[45] Y.X. Yeng, M. Ghebrebrhan, P. Bermel, W.R. Chan, J.D. Joannopoulos, M. Soljačić, I. Čelanović, Enabling high-temperature nanophotonics for energy applications, Proc. Natl. Acad. Sci. USA 109 (7) (2012) 2280–2285.
[46] V. Rinnerbauer, S. Ndao, Y.X. Yeng, J.J. Senkevich, K.F. Jensen, J.D. Joannopoulos, M. Soljačić, I. Čelanović, Large-area fabrication of high aspect ratio tantalum photonic crystals for high-temperature selective emitters, J. Vac. Sci. Technol. B 31 (1) (2013) 011802.
[47] V. Stelmakh, V. Rinnerbauer, R.D. Geil, P.R. Aimone, J.J. Senkevich, J.D. Joannopoulos, M. Soljačić, I. Čelanović, High-temperature tantalum tungsten alloy photonic crystals: Stability, optical properties, and fabrication, Appl. Phys. Lett. 103 (2013) 123903.
[48] J.B. Chou, Y.X. Yeng, A. Lenert, V. Rinnerbauer, I. Čelanović, M. Soljačić, E.N. Wang, S.-G. Kim, Design of wide-angle selective absorbers/emitters with dielectric filled metallic photonic crystals for energy applications, Opt. Express 22 (S1) (2014) A144–A154.
[49] Y.X. Yeng, J.B. Chou, V. Rinnerbauer, Y. Shen, S.-G. Kim, J.D. Joannopoulos, M. Soljačić, I. Čelanović, Global optimization of omnidirectional wavelength selective emitters/absorbers based on dielectric-fileld anti-reflection coated two-dimensional metallic photonic crystals, Opt. Express 22 (18) (2014) 21711–21718.
[50] D.L.C. Chan, M. Soljačić, J.D. Joannopoulos, Thermal emission and design in 2D-periodic metallic photonic crystal slabs, Opt. Express 14 (19) (2006) 8785–8796.
[51] M. Ghebrebrhan, P. Bermel, Y.X. Yeng, I. Čelanović, M. Soljačić, J.D. Joannopoulos, Tailoring thermal emission via q matching of photonic crystal resonances, Phys. Rev. A 83 (2011) 033810‘.
[52] M. Shimizu, A. Kohiyama, H. Yugami, Evaluation of thermal stability in spectrally selective few-layer metallo-dielectric structures for solar thermophotovoltaics, J. Quant. Spectrosc. Radiat. Transf. 212 (2018) 45–49.
[53] Gnanavel Vaidhyanathan Krishnamurthy, Manohar Chirumamilla, Surya Snata Rout, Kaline P. Furlan, Tobias Krekeler, Martin Ritter, Hans-Werner Becker, Alexander Yu Petrov, Manfred Eich, Michael Störmer, Structural degradation of tungsten sandwiched in hafnia layers determined by in-situ XRD up to 1520 °c, Nat. Sci. Rep. 11 (3330) (2021).
[54] V. Rinnerbauer, Y.X. Yeng, W.R. Chan, J.J. Senkevich, J.D. Joannopoulos, M. Soljačić, I. Čelanović, High-temperature stability and selective thermal emission of polycrystalline tantalum photonic crystals, Opt. Express 21 (9) (2013) 11482–11491.
[55] V. Liu, S. Fan, S^4: A free electromagnetic solver for layered periodic structures, Comput. Phys. Comm. 183 (2012) 2233–2244.
[56] F.L. Martínez, M. Toledano-Luque, J.J. Gandía, J. Cárabe, W. Bohne, J. Röhrich, E. Strub, I. Mártil, Optical properties and structure of HfO2 thin films grown by high pressure reactive sputtering, J. Phys. D: Appl. Phys. 40 (2007) 5256–5265.
[57] M.F. Modest, Radiative Heat Transfer, 3, Academic, Oxford, 2013.
[58] Markus Deserno, How to generate equidistributed points on the surface of a sphere, URL https://www.cmu.edu/biolphys/deserno/pdf/sphere_equi.pdf.
[59] W. Chan, R. Huang, C. Wang, J. Kassakian, J. Joannopoulos, Modeling low-bandgap thermophotovoltaic diodes for high-efficiency portable power generators, Sol. Energy Mater. Sol. Cells 94 (2010) 509–514.
[60] Savannah ALD System User Manual, Doc 19-29-01628 Rev. 2, Cambridge NanoTech / Veeco.